Dynamic visualization of surface acoustic waves on a two-dimensional phononic crystal

Dieter M. Profunser, Eiji Muramoto, Osamu Matsuda, and Oliver B. Wright*
Division of Applied Physics, Graduate School of Engineering, Hokkaido University, Sapporo 060-8628, Japan

Udo Lang
Center of Mechanics, ETH Zurich, 8092 Zurich, Switzerland

(Received 19 February 2009; revised manuscript received 6 May 2009; published 1 July 2009)

Surface acoustic wave propagation on a microscopic two-dimensional phononic crystal consisting of a square lattice of holes is imaged in two dimensions and in real time at frequencies up to 1 GHz by means of pulsed ultrashort optical excitation and detection. The acoustic dispersion relation obtained by spatiotemporal Fourier transforms shows the opening of stop bands at the zone boundaries for surface waves traveling parallel to the phononic crystal axes. We detect pronounced Bloch harmonics above the stop band, and reveal the spatial mode distributions at different frequencies. We also observe phonon collimation for frequencies at which the constant-frequency surfaces become square in shape.

DOI: 10.1103/PhysRevB.80.014301 PACS number(s): 63.20.D−, 77.65.Dq, 68.35.Iv, 62.65.+k

I. INTRODUCTION

Periodic elastic structures, or phononic crystals, have diverse applications for the control of propagating sound.[1,2] These materials, with one-, two- or three-dimensional periodicity in their acoustic impedance, possess stop bands where the elastic waves are heavily damped. The most prevalent examples are one-dimensional (1D) phononic crystals that take the form of interdigital transducers—periodic microscopic metal gratings on piezoelectric substrates—for generating and detecting surface acoustic waves (SAWs). SAWs, involving a strain field that is localized to within a distance of the order of the acoustic wavelength from the surface, are in widespread use in electric filtering and signal processing applications up to the GHz range.[3]

The promise of new types of acoustic filtering and sound control has also stimulated work on bulk,[4–6] plate,[7–11] or surface[12–19] acoustic waves in two-dimensional (2D) phononic crystals consisting of arrays of cylinders, spheres or holes, also down to microscopic scales. Progress has likewise been made in the field of three-dimensional (3D) phononic crystals, for example for the purpose of MHz sound focusing, GHz band-gap tuning or optical modulation.[20–23] These 2D and 3D structures show stop bands for bulk or surface acoustic waves, in some cases for any propagation direction. Among the measurement methods for characterizing phononic crystals, spatiotemporal scanning of the acoustic field is particularly promising because the acoustic dispersion relation can be simply obtained by the use of Fourier transforms.[24] Using this method, (1D) tracking of SAWs on a 2D phononic crystal[25] and 2D tracking of SAWs on a 1D phononic crystal[26] have been reported. However, the 2D spatial tracking of acoustic waves in a 2D phononic crystal has not. In this paper we achieve this by imaging SAWs on a microscopic 2D air-silicon phononic crystal, and thereby reveal its acoustic dispersion characteristics. Apart from the field of phononics, this work also has ramifications in photonics where analogous dispersive phenomena occur.

II. EXPERIMENT

Our 2D phononic crystal consists of an array of air-filled holes etched in a Si (100) substrate of thickness 0.46 mm using a DRIE (deep reactive ion etching) process. The holes have diameter $D \approx 12$ μm, and are oriented in a regular square lattice, with lattice constant $a \approx 15$ μm, that is aligned with respect to the underlying Si crystal so that the phononic lattice x and y directions are oriented along $[0\bar{1}\bar{1}]$ and $[01\bar{1}]$ (see Fig. 1). The hole depth was determined using scanning white light interferometry to be 10.5 μm. The filling fraction $\pi D^2/(4a^2)$ is 50%. The hole diameter and sepa-

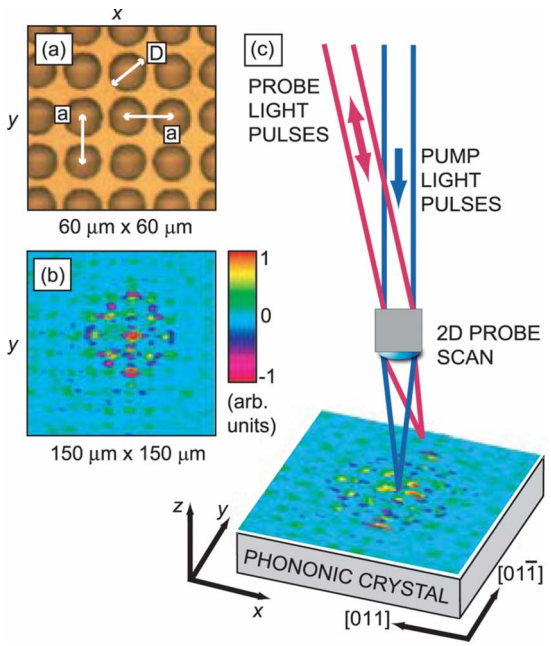

FIG. 1. (Color online) (a) Optical micrograph of the Si phononic crystal coated with a 40 nm gold layer. The hole diameter is $D = 12$ μm with lattice constant $a = 15$ μm. (b) SAW image at delay time $\tau = 7.4$ ns (c) Outline of experimental setup with SAW image at $\tau = 10.3$ ns.

ration are chosen to match as well as possible the excited acoustic wave vector spectrum while at the same time allowing sufficient optical access to the surface of the sample.[27] The hole depth is sufficient, for the range of surface acoustic wavelengths excited ($\lambda \sim 5-50$ μm), for the sample to act as a phononic crystal. After fabrication the crystal is coated with a 40 nm Au film for enhanced, uniform reflectivity and to allow efficient surface-localized thermoelastic excitation.[28] For the surface wave frequency range in question (100 MHz–1 GHz), this film thickness and the substrate thickness do not have a significant effect on the acoustic dispersion relation.

An optical micrograph of the sample is shown in Fig. 1(a). For surface wave imaging we use an optical pump and probe technique combined with a common-path interferometer based on a Sagnac configuration.[29] The normally incident subpicosecond-duration pump pulses from a Ti:sapphire laser at a repetition rate of 76.3 MHz have a wavelength of 400 nm after passing through a second-harmonic generation crystal. These pump pulses, corresponding to an absorbed fluence ~ 2 mJ cm^{-2}, thermoelastically excite broadband SAWs by focusing with a $\times 50$ microscope objective to a 2 μm diameter spot symmetrically positioned between four holes in the square lattice. SAW frequencies up to 1.1 GHz are generated, with the highest acoustic amplitudes occurring around 400 MHz (or a SAW wavelength of $\lambda \sim 10$ μm). The pump beam is chopped at 2 MHz for synchronous lock-in detection. We use two, delayed 800 nm optical probe pulses separated in time by 330 ps to detect an optical phase difference, $\Delta\phi$, proportional to the out-of-plane velocity of the sample surface. The probe beam is focused through the same objective lens to the same spot size as the pump. A scanning system based on tilting mirrors allows the probe spot to be raster scanned in two dimensions relative to that of the pump. The pump-probe delay time τ is incremented after each such spatial image has been acquired. The typical surface displacements measured are ~ 10 pm. Modes with predominantly shear-horizontal polarization (excited in the nonsymmetry directions on the phononic crystal) are only weakly detected through their out-of-plane displacement by our apparatus.[24]

III. RESULTS AND DISCUSSION

A. Real-time imaging and the dispersion for different propagation directions

A SAW image for a 150×150 μm^2 region, corresponding to a 10×10 hole array, is shown in Fig. 1(b) for $\tau = 7.4$ ns and in Fig. 1(c) for $\tau = 10.3$ ns. The SAW amplitude decreases rapidly with distance from the source at the center of the image because of acoustic scattering at the air holes and through geometric attenuation. The fourfold symmetry of the SAW wave fronts arises mainly from the hole array rather than from the underlying Si.[30] A complete temporal series of these SAW images consists of 32 frames within 13.1 ns. (An animation can be viewed in the supplementary material.[31]) The probe beam is only significantly reflected from the region between the holes, rather than from the holes themselves. This restricts the region of the sample available for imaging. In spite of this, we were able to adequately image the surface waves traveling in the regions between the holes.

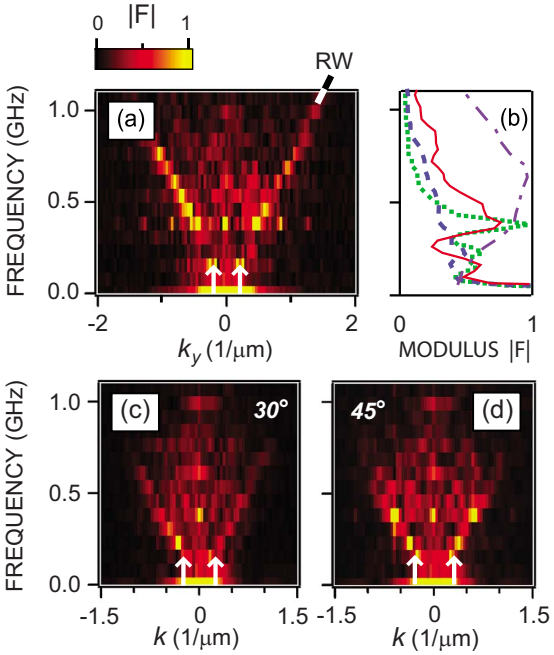

FIG. 2. (Color online) (a) Measured modulus of the spatiotemporal Fourier transform, plotted vs frequency and wave number for y-directed propagation. (b) Corresponding normalized modulus of the Fourier transform for the y direction (solid red line), $\theta = 30°$ (dashed blue line) and $\theta = 45°$ (dotted green line), plotted vs frequency on the same scale. Also plotted (dashed-dotted purple line) is the normalized modulus for an unpatterned region of the sample. [(c) and (d)] Measured modulus of the Fourier transform for $\theta = 30°$ and 45°, respectively. The upwardly directed arrows in (a), (c), and (d) represent the boundaries of the first BZ for the directions concerned.

The acoustic dispersion relation is obtained from a 2D spatial and a 1D temporal Fourier transform, with integrals taken, respectively, over the imaged area and one 13.1 ns period of the laser-pulse train.[24–26,32] The phononic lattice periodicity introduces Brillouin zone (BZ) boundaries in **k** space. In the x and y directions the first BZ boundaries are situated at wave numbers $k = \pm \pi/a = \pm 0.21$ μm^{-1}, where $a = 15$ μm. Because of the periodic excitation at the laser repetition rate of 76.3 MHz, only surface waves with integral multiples of this frequency are produced and recorded by the temporal Fourier transform. Sections of the f-k relation in different directions, where f is the frequency, are shown in Figs. 2(a), 2(c), and 2(d). In Fig. 2(a), corresponding to $k = k_y$ and $k_x = 0$, only one acoustic branch is discernable up to 1 GHz. We associate this branch with Rayleigh surface waves (labeled RW) with velocity ~ 4800 ms^{-1}, a value similar to the velocity, 5100 ms^{-1}, for x-directed Rayleigh modes (pseudosurface waves near this direction) on a bare Si substrate.[30,33] (Our thermoelastic source, placed symmetrically between four holes, does not excite pure shear-horizontal modes. The latter are in any case not detected with our out-of-plane motion detection.) One can also discern in Fig. 2(a) a region round 300 MHz where the propagation is

highly attenuated. The same effect is also observed in the x direction (not shown). Combined with evidence from the constant-frequency surfaces presented later, this attenuation suggests the presence of a phononic stop band for x- and y-directed propagation. A surface acoustic wave stop band for a similar deep-hole Si-air lattice of this type and filling factor was previously reported by Wu *et al.*[34] The effect of the finite hole depth in our sample presumably complicates the band structure in the same way as the finite thickness does for phononic crystal plates, in which stop bands have also been detected.[8,9]

Just above the observed stop band one can see in Fig. 2(a) striking periodic features in k_y separated by the reciprocal-lattice vector $2\pi\mathbf{j}/a$, where $\mathbf{j}$ is the unit vector in the y direction and $2\pi/a=0.42\ \mu\mathrm{m}^{-1}$. These are Bloch harmonics, arising because of the periodic potential. These were previously demonstrated for 1D phononic crystals with the same experimental technique,[26] and are also the subject of investigations in photonic crystals.[35–37] Bloch harmonics arise when expanding the surface disturbance $f(\mathbf{r},t)$ (i.e., the out-of-plane surface velocity) in the eigenmodes of the periodic structure, in this case a square lattice,[26,37]

$$f(\mathbf{r},t)=\mathrm{Re}\sum_n\int_{1\mathrm{st\ BZ}}A_n(\mathbf{k})\sum_{l,m}C_{n,l,m}(\mathbf{k})\exp\left[i\left(\mathbf{k}+\frac{2\pi l}{a}\mathbf{i}+\frac{2\pi m}{a}\mathbf{j}\right)\cdot\mathbf{r}-i\omega_n(\mathbf{k})t\right]d^2\mathbf{k},\qquad(1)$$

where $\omega_n(\mathbf{k})$ is the angular frequency, l and m are integers, and $\mathbf{i}$ is the unit vector in the x direction. The source functions $A_n(\mathbf{k})$, related to the optical excitation and detection, specify the amplitude of a Bloch eigenstate indexed by $\mathbf{k}$ inside the first BZ and by branch number n. The complex coefficients $C_{n,l,m}$ determine the amplitude of each Bloch harmonic, and depend on the scattering potential. In analogy to the case for 1D,[26] the spatiotemporal Fourier transform $F(\mathbf{k},\omega)$ of Eq. (1) is directly proportional to the product of $A_n(\mathbf{k}')$ and $C_n(\mathbf{k})=C_n(\mathbf{k}'+2\pi l\mathbf{i}/a+2\pi m\mathbf{j}/a)=C_{n,l,m}(\mathbf{k}')$, where $\mathbf{k}'$ is the equivalent wave vector in the first BZ. The reciprocal lattice in this case is also a square lattice, and the Bloch harmonics are therefore expected to form a square pattern in the constant-frequency surfaces of $F(\mathbf{k},\omega)$. Our experimental results on Bloch harmonics are discussed in more detail below when we present our results for these constant-frequency surfaces.

In Fig. 2(b) the normalized amplitude along the RW branch in Fig. 2(a) is represented by the solid line; a reduced amplitude in the region of the stop band is evident. For comparison purposes we also imaged an unpatterned region of the sample adjacent to the phononic crystal. In this case we observe a broad spectrum of frequencies peaked at $f\approx 0.7$ GHz ($k\approx 0.9\ \mu\mathrm{m}^{-1}$), as shown by the dashed-dotted line in Fig. 2(b). (A similar spectrum was found for other samples with the same optical spot sizes.[38]) This variation represents the source function $A_n(\mathbf{k})$ [where $\mathbf{k}=\mathbf{k}(\omega)$] for Rayleigh waves on the unpatterned region.

In other propagation directions in the phononic crystal, such as at angles $\theta=30°$ and 45° to the x direction, stop bands are not resolved, as one can understand from Fig. 2(b) for these two angles and from Figs. 2(c) and 2(d) for $\theta=30°$ and 45°, respectively. In Fig. 2(b) it is clear that the RW branches for 30° and 45° propagation, with corresponding velocities 4300 and 3900 ms^{-1}, have a lower relative amplitude at frequencies $f>0.6$ GHz than for the case of $\theta=0°$. This may not seem surprising given that the spaces between the holes provide avenues for relatively unimpeded RW propagation in the x and y directions when $\lambda\ll a$ [see Fig. 1(a)]. However, a more rigorous explanation is a collimation effect arising from the phononic band structure, discussed below in connection with the constant-frequency surfaces.

B. Constant-frequency surfaces

We were also able to derive experimental constant-frequency surfaces $|F(\mathbf{k},\omega)|$ for integral multiples of 76.3 MHz, as shown for five consecutive frequencies on the left-hand column of Figs. 3(a)–3(e). (A complete series of these surfaces up to 1.1 GHz can be viewed in the supplementary material.[31]) The right-hand column provides a guide to the origin of the features seen. The dashed lines indicate periodically arranged first BZs. The overlapping circles represent the effect of the periodic potential on the position of the expected features in reciprocal space when accounting for the Bloch harmonics for all BZs (not just the first). These circles arise from the assumption of an isotropic RW constant-frequency surface (the central circle) that is matched to the experimental results for the predominant x- or y-directed RW, and only provide a rough guide. The positions where the circles overlap should lead to enhanced features in the case of a weak periodic potential. An animation of the circles increasing in size when superposed on the various BZs can be viewed in the supplementary material.[31]

At 153 MHz, as shown in Fig. 3(a), the RW mode forms a central ring characteristic of Si (100).[30] This ring is also visible as a ghost shifted by the reciprocal-lattice vector in the $\pm x$ and $\pm y$ directions, owing to the effect of the Bloch harmonics (corresponding in position to the blue circles on the right). The slight asymmetry between the Bloch harmonics and other features in the x and y directions may be caused by some ellipticity in the optical pump spot shape or to residual misalignment in the position of the optical pump spot with respect to the phononic crystal lattice.

At 229 and 305 MHz, as shown in Figs. 3(b) and 3(c), the constant-frequency surface splits into four symmetric parts, and a stop band opens up near 305 MHz for RWs propagating within an angle $\Delta\theta_1/2\sim 10°$ to the $\pm x$ and $\pm y$ directions [Fig. 3(c)]. This behavior is consistent with the angular dependence of Fig. 2.

At 382 MHz, as shown in Fig. 3(d), a large square array of periodic dots appears superimposed on a rounded-square shaped constant-frequency surface. These dots are evidently Bloch harmonics, and correspond to the points where four circles of radius $2\pi/a(=0.42\ \mu\mathrm{m}^{-1})$ in $\mathbf{k}$ space overlap at a single point (see right-hand figure). This factor of four evidently contributes to their enhanced intensity. This overlap is responsible for the periodic features we noted in Fig. 2(a) just above the stop band for y-directed propagation. Repre-

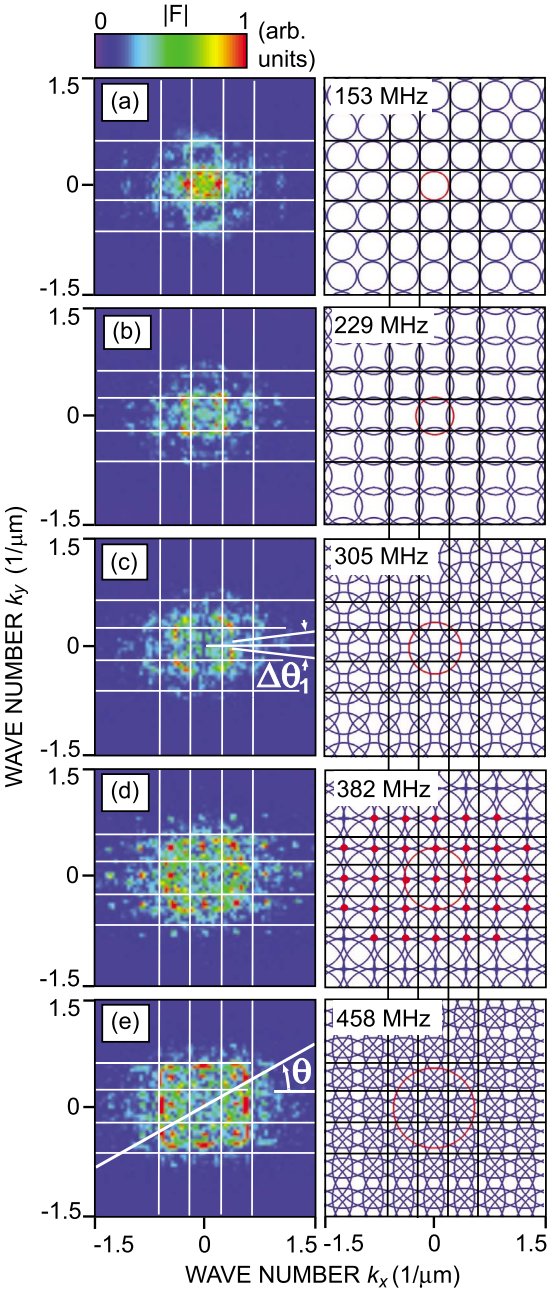

FIG. 3. (Color online) Constant-frequency surfaces from the modulus of spatiotemporal Fourier transforms for (a)–(e) 153, 229, 305, 382, and 458 MHz. The line grids indicate the periodically arranged first BZ. Identification of the features is aided by the construction on the right: the blue circles represent the RW Bloch harmonics corresponding to the central (red) circles. To the right of (d), dots have been added (in red) to correspond to the experimental features seen in (d).

sentative sections of the constant-frequency surface at 382 MHz that reveal the Bloch harmonics are given in Fig. 4. As is generally the case in periodic systems, one expects the effects of a weak periodic potential to be most strongly manifested in the region of the BZ boundaries, in this case when k_x or k_y touch the boundary of the second BZ. A periodic array of dots is evident to a lesser extent in Fig. 3(b) [and noticeable as the periodic features noted in Fig. 2(a)] where

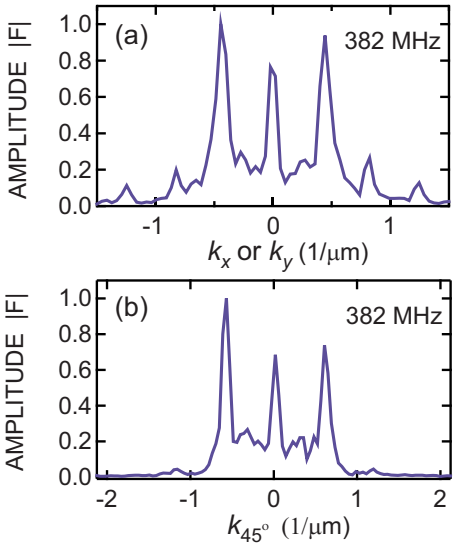

FIG. 4. (Color online) Cross sections through the center of the constant-frequency surface at 382 MHz showing Bloch harmonics: (a) average of x and y directions, and (b) average of the directions at 45° to x or y.

the circle radius is close to π/a and adjacent circles again overlap at a single point. A detailed quantitative explanation for these enhancements of the Bloch harmonics, not noted in similar experiments in 1D,[26] would require a detailed analysis of the phononic band structure.

For the higher frequency of 458 MHz, as shown by the plot of Fig. 3(e), the constant-frequency surface remains nearly square in shape, and shows significant amplitude in the higher order BZs. An approximately square constant-frequency surface for the case of bulk waves has been theoretically predicted for lattices of cylinders.[39–42] This square shape leads to regions of the constant-frequency surface in the x and y directions with low curvature. Wave vectors lying on these regions do not dephase during propagation through the crystal, resulting in nondivergent propagation, a phenomenon known as self-collimation that is analogous to phonon focusing in anisotropic homogeneous crystals.[43,44] This effect is largely responsible for the angular dependence in the intensities seen in Fig. 2. More evidence for this effect is given in the next subsection.

C. Spatial distributions at constant frequency

Further insight into these results can be obtained from the spatial distribution of the eigenmodes at each frequency $F(\mathbf{r},\omega)$ derived from the temporal Fourier transforms. The results for the same five frequencies as in Fig. 3 are shown in both amplitude $A=|F(\mathbf{r},\omega)|$ [(a)–(e)] and phase $\psi=\arg[F(\mathbf{r},\omega)]$ [(f)–(j)] in Fig. 5 for a 150×150 μm^2 region, each series plotted on identical scales. (A complete series of these plots can be viewed in the supplementary material.[31]) The position of the 10×10 array of holes is particularly clear from the regions of low amplitude in Fig. 5(a), and also shown for four adjacent holes in Figs. 5(b) and 6(b). The mode patterns at all these frequencies approximately show the fourfold symmetry of the phononic lattice. This is par-

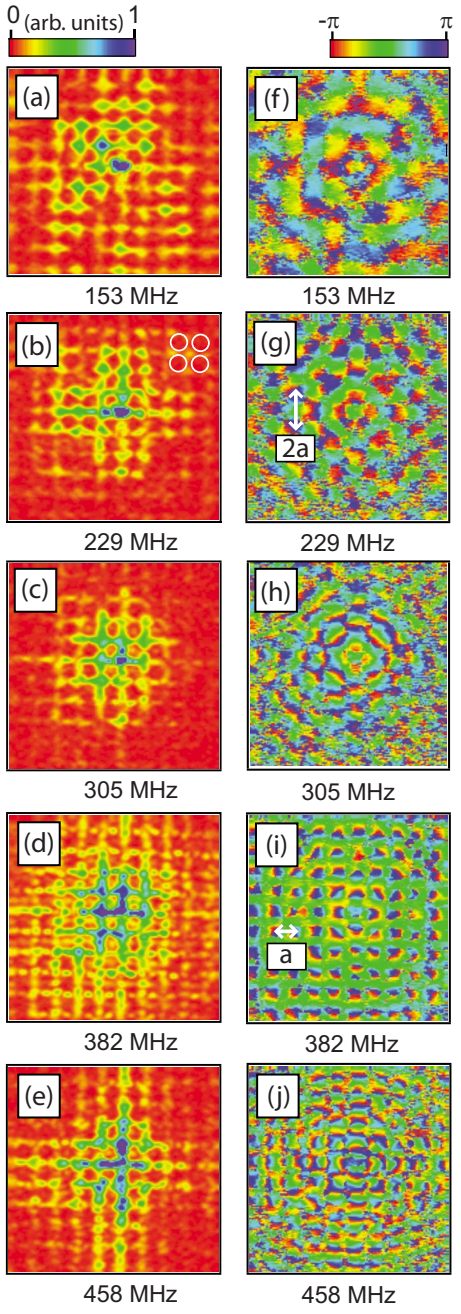

FIG. 5. (Color online) [(a)–(e)] Measured modulus A of the temporal Fourier transforms, plotted in real space over a 150 $\times 150$ μm^2 region at different frequencies. Identical scales are used in each case, so that the amplitude of the plots accurately represents the relative amplitudes observed in experiment. [(f)–(j)] Measured phase ψ of the temporal Fourier transforms.

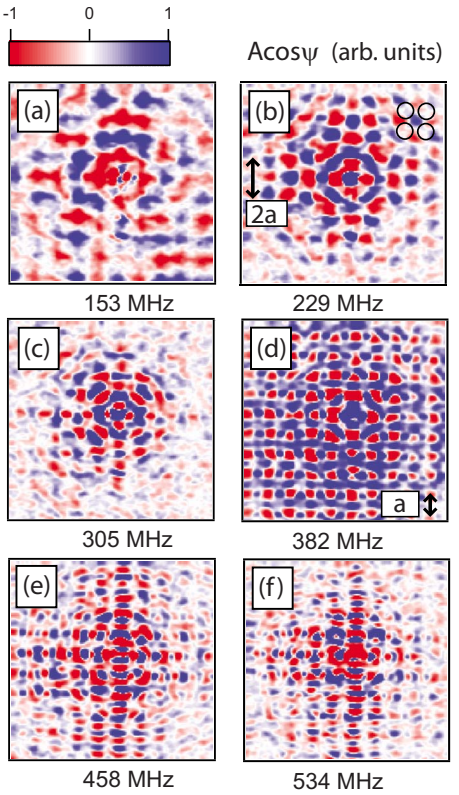

FIG. 6. (Color online) Measured real part $A \cos \psi$ of the temporal Fourier transforms at different acoustic frequencies, plotted in real space over a 150×150 μm^2 region. Identical scales are used in each case.

ticularly evident in the phase; as the frequency increases the patterns become finer since the wavelength decreases. The larger amplitudes seen near the center of each image for A are partially caused by the broadband response to the transient thermoreflectance and partially by the effects of geometrical attenuation associated with the spreading 2D wavepacket. These results for amplitude and phase at different frequencies can be effectively viewed as animations in the form $A \cos(\omega t + \psi)$.[31] Snapshots at six different frequencies of the quantity $A \cos \psi = \mathrm{Re}[F(\mathbf{r}, \omega)]$ are shown in Fig. 6. The advantage of viewing $A \cos \psi$ is that it represents the instantaneous phonon field at a specific time during a single cycle, and is a snapshot of what would be directly observed if the center of the phononic crystal was continuously excited at a constant frequency. As with the phase images, the patterns clearly show the dominant acoustic wavelengths at each frequency.

As expected from the form of the constant-frequency surface, at 153 MHz the phonon field retains an element of circular symmetry because of the relatively long wavelength ($\lambda \sim 3a$) compared to the hole spacing, as can be seen from the phase in Fig. 5(f) and from $A \cos \psi$ in Fig. 6(a) [and also at 76 MHz (Ref. 31)].

At 229 MHz, the wave number for the x direction is $k_x \approx \pm \pi / a (=0.21\ \mu m^{-1})$. The corresponding acoustic wavelength is $\lambda_x = 2a$. One can indeed see periodicity in the patterns of Figs. 5(b), 5(g), and 6(b) consistent with $\lambda_x = \lambda_y \approx 2a$: the maxima in amplitude occur at points approximately equidistant between four holes, and adjacent unit cells vibrate in antiphase. For the x and y directions this mode is a pure standing wave that satisfies the Bragg scattering condition.[45]

At 305 MHz, the effect of the directional stop band is to diminish the relative intensity of the phonon field in the $\pm x$ and $\pm y$ directions. The effect of this stop band is not as evident in real space as it is in $\mathbf{k}$ space [Fig. 3(c)]. A detailed prediction of the angular dependence of the phonon field

would require a detailed knowledge of the phononic band structure.

As explained above in relation to the Bloch harmonics of Fig. 3(d), an effect similar to that at 229 MHz arises at 382 MHz [Figs. 5(d), 5(i), and 6(d)]: at 382 MHz the **k** vector in the x or y directions or in the 45° directions is closely equal to a reciprocal-lattice vector ($\pm 2\pi\mathbf{i}/a$, $\pm 2\pi\mathbf{j}/a$, or $\pm 2\pi\mathbf{i}/a \pm 2\pi\mathbf{j}/a$). For example, the corresponding wave number in the x direction is $k_x \approx \pm 2\pi/a$ in the extended-zone scheme, with acoustic wavelength $\lambda_x = a$. Periodicity in the patterns of Figs. 5(d) and 5(i) consistent with $\lambda_x = \lambda_y \approx a$ is evident. Maxima in amplitude occur at points equidistant between any four holes, and subsidiary maxima occur at points equidistant between any two holes. These two series of maxima correspond to points oscillating in antiphase. To a good approximation this mode is a pure standing wave that satisfies the Bragg scattering condition for all propagation directions. Because of the nearly square shape of the constant-frequency surface at this frequency, this mode is equivalent to $\mathbf{k} \approx \mathbf{0}$ in the reduced-zone scheme (in which the $\omega - \mathbf{k}$ relation is folded back into the first BZ) for nearly all **k**. Analogous $\mathbf{k} = \mathbf{0}$ modes have also been observed in 1D and 2D surface phononic crystals.[46–48]

At 458 MHz and at 534 MHz [Figs. 6(e) and 6(f)], and also at 229 MHz [in Fig. 5(b)], phonon collimation in the x and y directions can be clearly seen. [This is particularly clear in the animations of $A\cos(\omega t + \psi)$.[31,49]] This effect has been experimentally observed in bulk phononic crystals.[40,42] The effect is also well known in photonic crystals, where it is known as photon focusing or self-collimation,[50] and is considered to be a promising method for guiding light beams.[51,52]

IV. CONCLUSIONS

In conclusion, by means of a dynamic imaging technique we have directly probed the eigenmodes and the dispersion relation, including a directional stop band, for surface wave propagation in a 2D phononic crystal consisting of a square array of finite-depth holes in a Si crystal. Moreover, we have revealed the presence of highly pronounced Bloch harmonics above the stop band, posing a challenge for quantitative theoretical interpretation. Another welcome advance would be the derivation of the constant-frequency surfaces for surface waves traveling over such a finite-depth square lattice array. More experimental investigations are also required to better understand the form of the constant-frequency surfaces. It would be interesting to carry out a further series of measurements to elucidate the effects of different hole depths. The present signal-to-noise ratio might also be improved by using elongated optical spots to excite surface waves in chosen directions. In addition, a finer frequency step could be obtained by the use of a laser of lower repetition rate in order to obtain a higher-definition measurement of the phononic band structure.

ACKNOWLEDGMENTS

D. M. Profunser acknowledges financial support from the Japanese Society for the Promotion of Science (JSPS). We thank Alex Maznev and Yukihiro Tanaka for valuable discussions.

*assp@kino-ap.eng.hokudai.ac.jp

[1] M. S. Kushwaha, Int. J. Mod. Phys. B **10**, 977 (1996).
[2] M. Sigalas, M. S. Kushwaha, E. N. Economou, M. Kafesaki, I. E. Psarobas, and W. Steurer, Z. Kristallogr. **220**, 765 (2005).
[3] F. S. Hickernell, in *Physical Acoustics*, edited by R. N. Thurston, A. D. Pierce, and E. P. Papadakis (Academic, London, 1999), Vol. 24, p. 135.
[4] J. O. Vasseur, P. A. Deymier, B. Chenni, B. Djafari-Rouhani, L. Dobrzynski, and D. Prevost, Phys. Rev. Lett. **86**, 3012 (2001).
[5] T. Gorishnyy, C. K. Ullal, M. Maldovan, G. Fytas, and E. L. Thomas, Phys. Rev. Lett. **94**, 115501 (2005).
[6] J. Baumgartl, M. Zvyagolskaya, and C. Bechinger, Phys. Rev. Lett. **99**, 205503 (2007).
[7] K. Kokkonen, M. Kaivola, S. Benchabane, A. Khelif, and V. Laude, Appl. Phys. Lett. **91**, 083517 (2007).
[8] J. O. Vasseur, A.-C. Hladky-Hennion, B. Djafari-Rouhani, F. Duval, B. Dubus, Y. Pennec, and P. A. Deymier, J. Appl. Phys. **101**, 114904 (2007).
[9] S. Mohammadi, A. A. Eftekhar, A. Khelif, W. D. Hunt, and A. Adibi, Appl. Phys. Lett. **92**, 221905 (2008).
[10] J. J. Chen, B. Bonello, and Z.-L. Hou, Phys. Rev. E **78**, 036609 (2008).
[11] R. Sainidou, B. Djafari-Rouhani, and J. O. Vasseur, Phys. Rev. B **77**, 094304 (2008).
[12] Y. Tanaka and S. I. Tamura, Phys. Rev. B **58**, 7958 (1998).
[13] Y. Tanaka and S. I. Tamura, Phys. Rev. B **60**, 13294 (1999).
[14] E. V. Tartakovskaya, Phys. Rev. B **62**, 11225 (2000).
[15] V. Laude, M. Wilm, S. Benchabane, and A. Khelif, Phys. Rev. E **71**, 036607 (2005).
[16] T. T. Wu, L. C. Wu, and Z. G. Huang, J. Appl. Phys. **97**, 094916 (2005).
[17] S. Benchabane, A. Khelif, J.-Y. Rauch, L. Robert, and V. Laude, Phys. Rev. E **73**, 065601(R) (2006).
[18] D. Zhao, Z. Liu, C. Qiu, Z. He, F. Cai, and M. Ke, Phys. Rev. B **76**, 144301 (2007).
[19] Y. Tanaka, T. Yano, and S. Tamura, Wave Motion **44**, 501 (2007).
[20] S. Yang, J. H. Page, Z. Y. Liu, M. L. Cowan, C. T. Chan, and P. Sheng, Phys. Rev. Lett. **93**, 024301 (2004).
[21] J. H. Jang, C. K. Ullal, T. Gorishnyy, V. V. Tsukruk, and E. L. Thomas, Nano Lett. **6**, 740 (2006).
[22] W. Cheng, J. J. Wang, U. Jonas, G. Fytas, and N. Stefanou, Nature Mater. **5**, 830 (2006).
[23] A. V. Akimov, Y. Tanaka, A. B. Pevtsov, S. F. Kaplan, V. G. Golubev, S. Tamura, D. R. Yakovlev, and M. Bayer, Phys. Rev. Lett. **101**, 033902 (2008).
[24] Y. Sugawara, O. B. Wright, and O. Matsuda, Appl. Phys. Lett. **83**, 1340 (2003).

[25] X. Y. Zhang, T. Jackson, E. Lafond, P. Deymier, and J. Vasseur, Appl. Phys. Lett. **88**, 041911 (2006).
[26] D. M. Profunser, O. B. Wright, and O. Matsuda, Phys. Rev. Lett. **97**, 055502 (2006).
[27] The constraint concerning the limited space between the holes could be removed by filling the holes with another material and ensuring the whole of the top surface were flat, but this process for such microscopic samples would require a much more complicated fabrication technique, involving, for example, chemical mechanical polishing.
[28] The thermal-expansion coefficient of Au is approximately five times greater than that of Si, whereas the reflection coefficients at the laser excitation wavelength are comparable.
[29] T. Tachizaki, T. Muroya, O. Matsuda, Y. Sugawara, D. H. Hurley, and O. B. Wright, Rev. Sci. Instrum. **77**, 043713 (2006).
[30] R. E. Vines, M. R. Hauser, and J. P. Wolfe, Z. Phys. B: Condens. Matter **98**, 255 (1995).
[31] See EPAPS Document No. E-PRBMDO-79-036921 for the animations. For more information on EPAPS, see http://www.aip.org/pubservs/epaps.html.
[32] B. Bonello, C. Charles, and F. Ganot, Appl. Phys. Lett. **90**, 021909 (2007).
[33] T. Aono and S. Tamura, Phys. Rev. B **55**, 6754 (1997).
[34] T. T. Wu, Z. G. Huang, and S. Y. Liu, Z. Kristallogr. **220**, 841 (2005).
[35] M. Sandtke and L. Kuipers, Phys. Rev. B **77**, 235439 (2008).
[36] R. J. P. Engelen, D. Mori, T. Baba, and L. Kuipers, Phys. Rev. Lett. **102**, 023902 (2009).
[37] R. J. P. Engelen, Y. Sugimoto, H. Gersen, N. Ikeda, K. Asakawa, and L. Kuipers, Nat. Phys. **3**, 401 (2007).
[38] Y. Sugawara, O. B. Wright, O. Matsuda, M. Takigahira, Y. Tanaka, S. Tamura, and V. E. Gusev, Phys. Rev. Lett. **88**, 185504 (2002).
[39] L.-S. Chen, C.-H. Kuo, and Z. Ye, Appl. Phys. Lett. **85**, 1072 (2004).
[40] V. Espinosa, V. J. Sánchez-Morcillo, K. Staliunas, I. Pérez-Arjona, and J. Redondo, Phys. Rev. B **76**, 140302(R) (2007).
[41] I. Pérez-Arjona, V. J. Sánchez-Morcillo, J. Redondo, V. Espinosa, and K. Staliunas, Phys. Rev. B **75**, 014304 (2007).
[42] J. Shi, S.-C. S. Lin, and T. J. Huanga, Appl. Phys. Lett. **92**, 111901 (2008).
[43] H. J. Maris, Phys. Rev. B **28**, 7033 (1983).
[44] A. G. Every, Phys. Rev. B **34**, 2852 (1986).
[45] C. Kittel, *Introduction to Solid State Physics* (Wiley, New York, 2005), p. 93.
[46] C. Giannetti, B. Revaz, F. Banfi, M. Montagnese, G. Ferrini, F. Cilento, S. Maccalli, P. Vavassori, G. Oliviero, E. Bontempi, L. E. Depero, V. Metlushko, and F. Parmigiani, Phys. Rev. B **76**, 125413 (2007).
[47] J.-F. Robillard, A. Devos, I. Roch-Jeune, and P. A. Mante, Phys. Rev. B **78**, 064302 (2008).
[48] A. A. Maznev, Phys. Rev. B **78**, 155323 (2008).
[49] At higher frequencies, collimation in the *y* direction dominates, presumably owing to pump spot ellipticity or misalignment.
[50] P. Etchegoin and R. T. Phillips, Phys. Rev. B **53**, 12674 (1996).
[51] P. T. Rakich, M. S. Dahlem, S. Tandon, M. Ibanescu, M. Soljacic, G. S. Petrich, J. D. Joannopoulos, L. A. Kolodziejski, and E. P. Ippen, Nature Mater. **5**, 93 (2006).
[52] D. W. Prather, S. Shi, J. Murakowski, G. J. Schneider, A. Sharkawy, C. Chen, B. Miao, and R. Martin, J. Phys. D **40**, 2635 (2007).